The Astrophysical Journal, 999:74 (9pp), 2026 March 1 https://doi.org/10.3847/1538-4357/ae3fa2

Stellar Populations in the Extreme Outer Halo of the Spiral Galaxy M96

J. Christopher Mihos[1], Patrick R. Durrell[2], Brian Malkan[1], and Aaron E. Watkins[3]
[1] Department of Astronomy, Case Western Reserve University, Cleveland, OH 44106, USA
[2] Department of Physics, Astronomy, Geology, and Environmental Sciences, Youngstown State University, Youngstown, OH 44555, USA
[3] Centre for Astrophysics Research, University of Hertfordshire, College Lane, Hatfield, AL10 9AB, UK
Received 2025 September 15; revised 2026 January 13; accepted 2026 January 28; published 2026 February 25

Abstract

We use deep Hubble Space Telescope imaging to study stellar populations in the outer halo of the spiral galaxy M96, located in the dynamically active Leo I galaxy group. Our imaging targets two fields at a projected distance of 50 kpc from the galaxy's center, with a 50% photometric completeness limit of F814W = 28.0—nearly 2 magnitudes below the tip of the red giant branch (RGB). In both fields, we clearly detect red giant stars in M96's halo, with a space density that corresponds to an equivalent broadband surface brightness of $\mu_V \approx 31.7$ mag arcsec^{-2}. We find little evidence for any differences in the spatial density or color of the RGB stars in the two fields. Using isochrone matching, we derive a median metallicity for the red giants of $[M/H] = -1.36$, with an interquartile spread of ± 0.75 dex. Adopting a power-law radial density profile, we also derive a total halo mass of $M_h = 7.8^{+17.4}_{-4.9} \times 10^9 M_\odot$, implying a stellar halo mass fraction of $M_{*,\rm halo}/M_{*,\rm tot} \approx 15^{+33}_{-9}$%—on the high end for spiral galaxies, but with significant uncertainty. Finally, we find that M96 appears offset from the stellar halo mass–metallicity relationship for spirals, with a halo that is distinctly metal-poor for its halo mass. While a variety of systematic effects could have conspired to drive M96 off this relationship, if confirmed our results may argue for a markedly different accretion history for M96 compared to other spirals in the nearby Universe.

Unified Astronomy Thesaurus concepts: Galaxy stellar halos (598); Stellar populations (1622); Spiral galaxies (1560)

1. Introduction

The stellar halos of spiral galaxies contain a wealth of information about the accretion history of their host galaxies. While some fraction of a galaxy's stellar halo is built up in situ, halos continue to grow through the continual accretion and stripping of satellite galaxies over time (e.g., J. S. Bullock & K. V. Johnston 2005; A. S. Font et al. 2006; G. De Lucia & A. Helmi 2008; A. P. Cooper et al. 2010; A. J. Deason et al. 2016). These accretion events deposit stars with a range of metallicities and ages into the halo (V. Belokurov et al. 2006; R. A. Ibata et al. 2014; N. F. Martin et al. 2014, 2022; A. Bonaca & A. M. Price-Whelan 2025), leading to significant spatial and kinematic substructure in the stellar halo, which slowly mixes away over time. These accretion signatures are often most readily seen in the outer halos of galaxies ($\gtrsim$20–30 kpc), where the dynamical times are long and the contrast with the light of the host galaxy is greater.

While the stellar halos of the Milky Way and Andromeda have been studied extensively over time (e.g., R. Ibata et al. 2001, 2007; D. Carollo et al. 2007, 2010; A. W. McConnachie et al. 2009, 2018; K. M. Gilbert et al. 2012, 2014; R. A. Ibata et al. 2014; D. Crnojević 2017; C. Conroy et al. 2019; I. Ogami et al. 2025), it is only in recent years that observations have begun to probe the stellar halos around more distant spiral galaxies. Deep low-surface-brightness imaging has revealed a myriad of tidal streams embedded in the halos of massive spirals (e.g., D. Malin & B. Hadley 1997; Z. Shang et al. 1998; D. Martínez-Delgado et al. 2010, 2023; T. S. Chonis et al. 2011; A. Merritt et al. 2016) tracing recent accretion events that continue to build their stellar halos. Meanwhile, imaging of the discrete stellar populations in other galaxy halos from the Hubble Space Telescope (HST; and, for nearby galaxies, ground-based observatories) has begun to probe the metallicities (and, in some cases, ages) of stars in the halos of large spiral galaxies beyond the Local Group (M. Mouhcine et al. 2005a, 2005b; M. K. Barker et al. 2009; M. Rejkuba et al. 2009; P. R. Durrell et al. 2010; J. Bailin et al. 2011; D. J. Radburn-Smith et al. 2011; A. Monachesi et al. 2016; R. E. Cohen et al. 2020; A. Smercina et al. 2020; K. Gozman et al. 2023).

These studies have found a wide diversity of halo properties, with halo stellar-mass fractions ($M_{*,\rm halo}/M_{*,\rm gal}$) ranging from <1% for M101 (A. Merritt et al. 2016; I. S. Jang et al. 2020; C. Gilhuly et al. 2022) to 2%–3% for the Milky Way and M81 (B. Harmsen et al. 2017; A. J. Deason et al. 2019; J. T. Mackereth & J. Bovy 2020; A. Smercina et al. 2020) to over $\approx$ 10% for other luminous spirals (E. F. Bell et al. 2017; B. Harmsen et al. 2017; A. Smercina et al. 2022). Halo stellar populations also show a wide range of metallicity, ranging from $[M/H] = -2.0$ to -0.1 (M. Mouhcine et al. 2005a, 2007; J. S. Kalirai et al. 2006; P. R. Durrell et al. 2010; A. Monachesi et al. 2016; B. Harmsen et al. 2017; R. E. Cohen et al. 2020; J. Kang et al. 2020; K. M. Gilbert et al. 2022; A. Smercina et al. 2022; K. Gozman et al. 2023), and appear generally old (>8 Gyr) but with some evidence for intermediate-age populations as well (L. Greggio et al. 2014; M. Rejkuba et al. 2022; B. Harmsen et al. 2023).

Taken together, these studies have revealed a striking and rather tight correlation between the stellar halo mass and halo metallicity in spiral galaxies (E. F. Bell et al. 2017; B. Harmsen et al. 2017; A. Smercina et al. 2022). Galaxies with anemic stellar halos have relatively low halo metallicities, while those with more luminous stellar halos show much higher halo

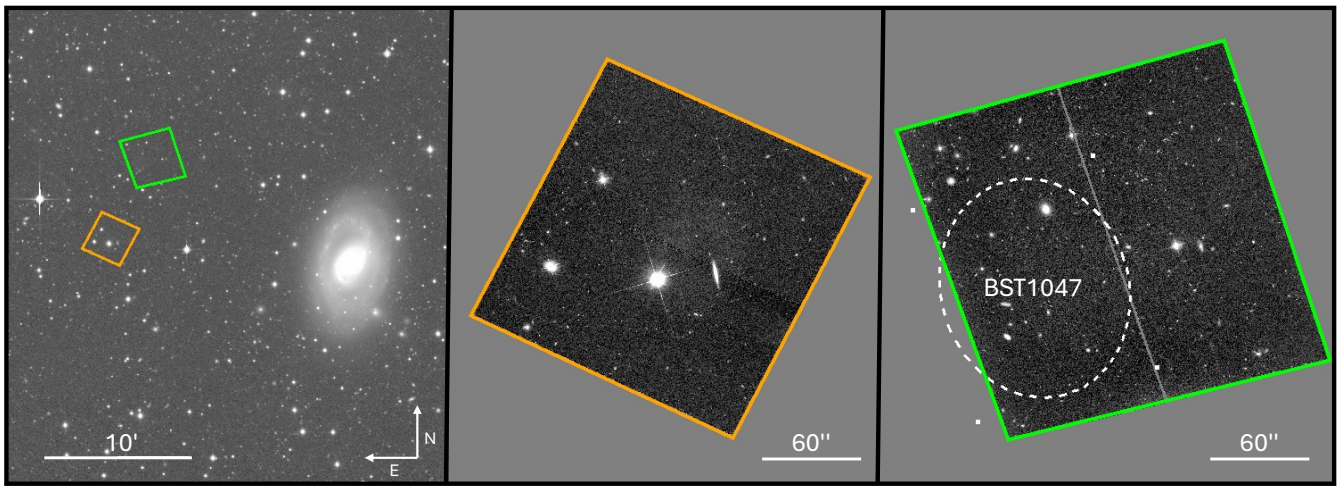

Figure 1. Placement of the WFC3 and ACS imaging fields. The left panel shows the ACS (green) and WFC3 (orange) footprints overlaid on the *B*-band imaging of M96 from A. E. Watkins et al. (2014). The WFC3 and ACS images are shown in the center and right panels, respectively. The dotted ellipse in the ACS image shows the location of the ultradiffuse galaxy BST1047 (J. C. Mihos et al. 2024). The ACS field lies at a projected distance of 15.′2 (48.6 kpc) from the center of M96, while the WFC3 field lies at a distance of 16.′3 (52.2 kpc). In all images, north is up and east is to the left.

metallicities. These results suggest that the properties of galaxy stellar halos are most strongly sensitive to the mass(es) of the most massive merger(s) in the galaxy's past accretion history, a behavior also seen in galaxy formation simulations (J. S. Bullock & K. V. Johnston 2005; A. P. Cooper et al. 2010; A. J. Deason et al. 2016; R. D'Souza & E. F. Bell 2018a; L. M. Elias et al. 2018; A. Monachesi et al. 2019; A. Fattahi et al. 2020). In this context, the Milky Way and Andromeda appear to represent opposite extremes on the scale of accretion-driven halo properties. Andromeda's stellar halo is massive ($M_{*,\rm halo} \sim 10^{10} M_{\odot}$; R. A. Ibata et al. 2014), high in stellar metallicity, and contains a wealth of complex substructure signifying an active accretion history (R. Ibata et al. 2001, 2004, 2007; M. Tanaka et al. 2010; K. M. Gilbert et al. 2012, 2014; R. A. Ibata et al. 2014; R. D'Souza & E. F. Bell 2018b; A. W. McConnachie et al. 2018; A. Dey et al. 2023). In contrast, the halo of the Milky Way is lower in stellar mass ($\sim 10^{9} M_{\odot}$; A. J. Deason et al. 2019; J. T. Mackereth & J. Bovy 2020) and metallicity, and while it contains numerous accretion signatures as well (e.g., V. Belokurov et al. 2006, 2018; A. Helmi et al. 2018; A. Helmi 2020; R. P. Naidu et al. 2020; A. J. Deason & V. Belokurov 2024, and references within), they tend to be lower in luminosity than those found in Andromeda. A variety of arguments suggest that the Milky Way has had a much more quiescent accretion history than Andromeda, possibly leading to the stark differences in their stellar halos (e.g., A. J. Deason et al. 2013; A. Pillepich et al. 2014; R. D'Souza & E. F. Bell 2018a; D. Sotillo-Ramos et al. 2022; E. Wempe et al. 2025).

If accretion dominates the properties of stellar halos around galaxies, differences in local environments may lead to the evolution of, or scatter in, the stellar halo mass–metallicity relationship, as ongoing interactions and accretion continue to build galaxy halos. Within this context, here we study stellar populations in the outer halo of the spiral galaxy M96 (NGC 3368) at a distance of 11 Mpc (J. A. Graham et al. 1997; M. G. Lee & I. S. Jang 2016). M96 is the most luminous spiral in the Leo I galaxy group—a group with a complex dynamical history. The group's massive elliptical M105 (NGC 3379) is surrounded by the extended Leo H I Ring (S. Schneider 1985; S. E. Schneider et al. 1986), possibly formed during an interaction with M96 (L. Michel-Dansac et al. 2010). M96 itself shows a distorted outer H I disk and is linked to the Leo Ring by a bridge of H I gas (T. Oosterloo et al. 2010). A number of H I clouds, possibly tidal in origin, are found between M96 and M95 (R. Taylor et al. 2022), the other large spiral in the group, and the group is also home to the gas-rich ultradiffuse galaxy BST1047+1156 (J. C. Mihos et al. 2018, 2024), likely spawned from the tidal debris connecting M96 and the Leo Ring. M96 thus provides an interesting opportunity to study the stellar halo of a galaxy in a dynamically active group.

In this study, we use deep HST imaging to image two fields in M96's outer halo, at a projected distance of ≈ 50 kpc from the center of the galaxy. Our imaging extends nearly 2 magnitudes below the tip of the red giant branch (TRGB), and we clearly detect RGB stars in both fields. We use the properties of this RGB population to derive the galaxy's stellar halo mass and metallicity and to show that M96 appears an outlier in the mass–metallicity relationship derived for other spiral galaxy halos, having a distinctly metal-poor halo despite its relatively large halo mass.

2. Observational Data

We imaged fields in the halo of M96 as part of our Hubble program GO-16762, to study the resolved stellar populations in the ultradiffuse galaxy BST1047+1156 (hereafter, BST1047; J. C. Mihos et al. 2018, 2024). When taking those data, we placed BST1047 on the eastern half of the Advanced Camera for Surveys (ACS) field (leaving the western half empty to sample a local background), while also using the WFC3 camera in parallel to image an adjacent field. These two fields, shown in Figure 1, lie at a projected distance of 15.′2 (ACS) and 16.′3 (WFC3) from the center of M96, sampling the stellar populations in M96's halo at a projected physical distance of ≈ 50 kpc (using the adopted 11.0 Mpc distance to the Leo I group; J. A. Graham et al. 1997; M. G. Lee & I. S. Jang 2016).

Both fields were imaged in the F606W and F814W filters over the course of 15 orbits. For the ACS field, the total exposure times were 16,458 s (F606W) and 16,590 s (F814W),

while the exposure times for the WFC3 field were 17,500 s (F606W) and 18,750 s (F814W). Two exposures were taken in each orbit, and within each visit we utilized a small ($\sim$0.″2) dither between exposures to aid in subpixel sampling of the imaging. Larger dithers ($\sim$1″) were made between visits to avoid artifacts on the detectors and to facilitate efficient cosmic-ray removal. We used the `drizzlepac` package to construct deep drizzled images of each field. Before drizzling, we used `tweakreg` to precisely align the world coordinate systems of the different images, using point sources on the individual `flc` images, then we used `astrodrizzle` to create stacked F606W and F814W images of each field; these stacked images are shown in Figure 1.

Rather than doing photometry on the drizzled stacks, we use the stacks as reference images to identify point sources in each field, then use the software package DOLPHOT (an updated version of HSTPhot; A. E. Dolphin 2000) to perform point-source photometry of these point sources on the individual charge-transfer-corrected `flc` images. Here, we give a brief summary of the DOLPHOT photometric analysis; complete details of the process can be found in J. C. Mihos et al. (2024) for the ACS imaging, and our analysis of the WFC3 imaging follows that process closely.

We begin the data reduction by preprocessing the images using the DOLPHOT `acsmask` and `wfc3mask` tasks to apply bad-pixel masks and pixel-area masks to each image, then we use `splitgroups` and `calcsky` to break each image up into the individual instrumental chips and calculate a preliminary background sky map for each chip image. In each field, we then use DOLPHOT to perform object detection and photometry simultaneously on the individual `flc` images, using the deep F814W drizzled image stack as the reference. The instrumental magnitudes were then converted to the VEGAMAG photometric system using updated zero-points from the ACS zero-point calculator.[4] We also use DOLPHOT to inject and measure 100,000 artificial stars (over the magnitude range $22 < \mathrm{F606W} < 30$ and color range $-0.5 < \mathrm{F606W} - \mathrm{F814W} < 2.0$) in each of the ACS and WFC3 images, in order to characterize the limiting depth of the images as well as any photometric bias in the derived magnitudes. All photometry reported here uses the VEGAMAG system, corrected for foreground Galactic extinction using $A_{\mathrm{F606W}} = 0.062$, $A_{\mathrm{F814W}} = 0.038$ (E. F. Schlafly & D. P. Finkbeiner 2011).

To achieve the cleanest, most accurate photometric catalogs of point sources in our deep imaging, we apply a variety of cuts to the DOLPHOT photometric catalogs. First, we use Astropy's `photutils/segmentation` task (L. Bradley et al. 2025) to identify and mask large objects in the field (bright foreground stars and background galaxies), then reject sources found within this mask. We also mask regions near the chipgaps on the ACS and WFC3 detectors where the signal-to-noise ratio (S/N) is reduced by dithering.

We next use the photometric information provided by DOLPHOT to further clean the photometry. Good sources need to be DOLPHOT TYPE=1 ("good star") with minimal crowding (CROWD < 0.25) and have S/N > 3.5 and goodness of fit CHI < 2.4 in both the F606W and F814W filters. We also apply a magnitude-dependent cut on the SHARP parameter to reduce the severe contamination due to background sources at magnitudes fainter than F814W ≈ 26. Following our earlier studies of resolved stellar populations in Leo, Virgo, and the M101 group (J. C. Mihos et al. 2018, 2022, 2024), we use a functional form for the cut of $|\mathrm{SHARP}| < \mathrm{SHARP0} + 0.3e^{(m-m_{\mathrm{crit}})}$. Due to the differences in pixel scale and depth between the imaging of the different cameras and filters, the values of the parameters can be a function of both camera and filter. For ACS, we use the same parameters used in our earlier analysis of the data (J. C. Mihos et al. 2024):
SHARP0 = 0.04, $m_{\mathrm{crit,F606W}} = 29.5$, $m_{\mathrm{crit,F814W}} = 28.7$. Based on our artificial star tests, we found that point sources in the WFC3 imaging appeared to show slightly nonzero SHARP values, so we adjusted the WFC3 SHARP0 cut parameter to SHARP0 = 0.06, broadening the SHARP selection slightly, but otherwise we left the m_{crit} parameters unchanged.

We used the artificial star tests to characterize the limiting depth (defined as the 50% recovery rate) and systematic biases in the DOLPHOT photometry. We process the artificial stars using the same selection cuts used for the real data, and we extract the completeness fraction, mean error, and systematic shift in magnitude and color as a function of both the F814W magnitude and F606W − F814W color. Because of our joint selection in F606W and F814W magnitudes, completeness is a function of both magnitude and color. For the ACS imaging, the 50% completeness limit is F814W = 28.2 at blue colors (at F606W − F814W = 0.0) and rises to F814W = 27.8 in the red (at F606W − F814W = 1.0). For the WFC3 imaging, the 50% completeness limits are F814W = 28.2 (blue) and 28.0 (red). At brighter magnitudes (F814W $\lesssim$ 27), we see no systematic shifts in the derived magnitudes or colors, but at fainter magnitudes the DOLPHOT photometry is measured as systematically too faint, by about 0.1 mag in ACS and by as much as 0.15–0.2 mag in WFC3. These shifts are consistent with our previous analysis of deep HST imaging (J. C. Mihos et al. 2018, 2022, 2024), and the systematics are similar in both F606W and F814W, such that the derived F606W − F814W colors show smaller systematic offsets. In particular, in the region defining red giant stars in the halo of M96 (see Section 3), the shifts are $\approx$0.05 mag in F814W magnitude and 0.03 or less in F606W − F814W color.

Finally, to avoid contamination from stellar populations in the ultradiffuse dwarf galaxy BST1047 (J. C. Mihos et al. 2018, 2024), we need to mask that galaxy from our ACS photometry. We construct a large elliptical mask on the eastern side of the ACS field (see Figure 1) that spans the entirety of BST1047. The mask covers 36% of the ACS field, reducing its effective area to 26,400 arcsec^2, comparable to that of the full WFC3 field (27,670 arcsec^2).

3. Analysis

We show the color–magnitude diagrams (CMDs) for point sources in the ACS and WFC3 fields in Figure 2. For comparison, Figure 2 also shows a comparably deep CMD for point sources derived from imaging of the A2744 Flanking Field (hereafter, A2744FF; J. M. Lotz et al. 2017). As described in J. C. Mihos et al. (2018), the A2744 imaging provides a good control field for assessing the expected background counts as a function of color and magnitude in our deep studies of resolved stellar populations in nearby galaxies such as M96. We analyze that dataset using the same techniques described above—using DOLPHOT to extract

[4] https://acszeropoints.stsci.edu/

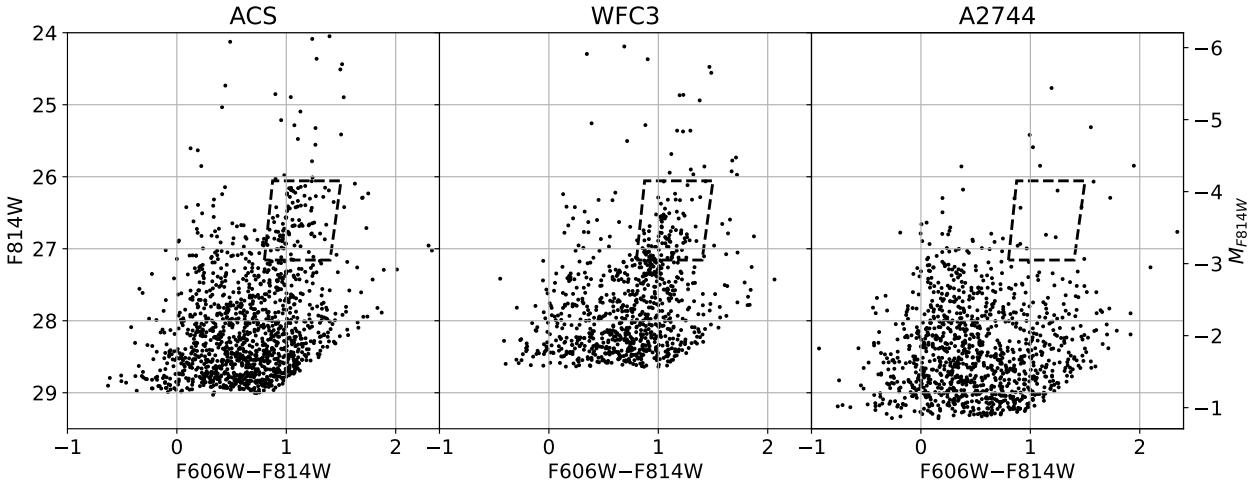

Figure 2. CMDs for our ACS (left) and WFC3 (center) fields, along with a similarly extracted CMD for A2744FF (right). The latter dataset has been randomly subsampled down by a factor of 0.6 to account for its larger area (see the text). The dashed box in each CMD shows the region expected to be populated by metal-poor red giant stars at the distance of M96.

point-source photometry, then applying the same photometric cuts as for the M96 halo fields analyzed here (for more details, see J. C. Mihos et al. 2018). We note, however, two differences between the A2744FF imaging and our M96 halo fields: that the A2744FF imaging has a ∼60% larger area than the WFC3 or (masked) ACS fields; and that it sits at higher Galactic latitude ($b_{A2744} = -81°$, compared to $b_{M96} = +57°$). To account for the difference in field area, we randomly select 60% of the sources in the A2744FF dataset to plot, so that the density of sources shown on the CMD is comparable to that for our M96 ACS and WFC3 fields.

The dashed boxes in Figure 2 show the expected location of metal-poor ([M/H] $\lesssim -0.7$) red giant stars at the distance of M96. In that region of the CMDs, we see a clear excess of sources in both the ACS and WFC3 fields compared to the A2744FF data. These sources have a spatial density of 13.0 arcmin^{-2} in the ACS field and 12.7 arcmin^{-2} in the WFC3 field, compared to only 1.3 arcmin^{-2} in the A2744FF data. We expect little contamination from Milky Way stars; using the Besançon Galactic structure model (A. C. Robin et al. 2003), the density of Milky Way halo stars in this region of the CMDs is only 0.25 arcmin^{-2}. Thus, we have a clear detection of M96 halo stars with similar spatial density in both the ACS and WFC3 fields.

Contamination from stellar populations associated with BST1047 also appears unlikely. As shown in J. C. Mihos et al. (2024), BST1047 shows prominent red and blue helium-burning sequences that trace a weak burst of star formation in that object approximately 100–200 Myr ago. However, we see no evidence for this population in our M96 halo photometry; the density of sources in the CMD at bluer colors, where blue helium-burning stars would lie ($0.0 \leqslant$ F606W − F814W $\leqslant 0.6$ and $26 \leqslant$ F814W $\leqslant 27$), is comparable in both the ACS and WFC3 fields (3.5 and 2.4 arcmin^{-2}, respectively) and similar to that observed in the A2744FF CMD (3.0 arcmin^{-2}). Furthermore, as seen in Figure 3, the spatial distribution of sources in the RGB box shows no clustering around BST1047 in the ACS field, arguing that these sources are not red helium-burning stars in BST1047. We also note that subdividing the RGB population by color or luminosity does not change the overall spatial distributions of the selected sources shown in Figure 3. Finally, contamination by old stellar populations

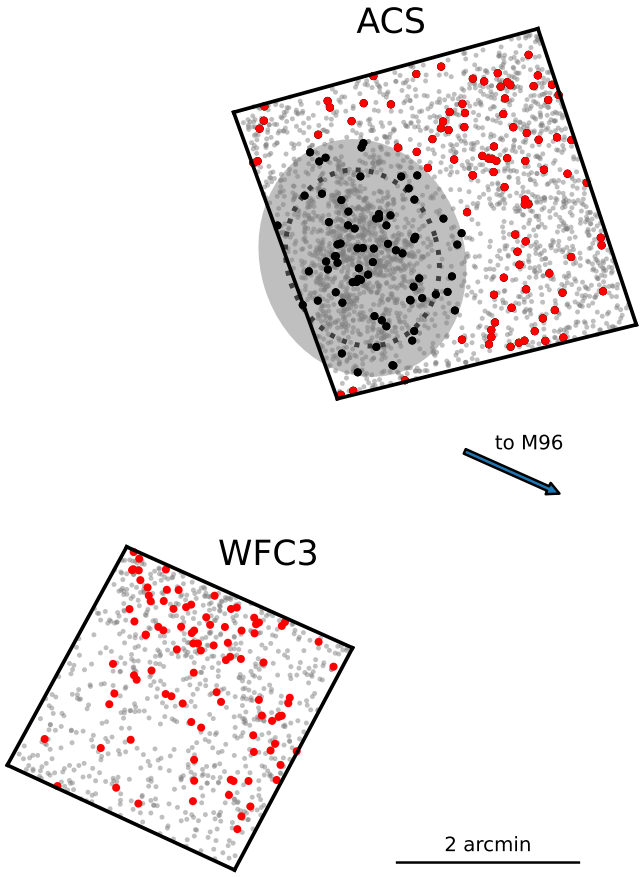

Figure 3. Spatial distributions of the stellar populations in the ACS and WFC3 fields. The light gray points show all detected point sources, while the red dots show red giant stars selected from the dashed RGB boxes in Figure 2. In the ACS field, the dotted oval shows the region containing BST1047, and the shaded oval shows the (slightly expanded) mask to exclude sources in this region. However, for clarity in showing the overall distribution of RGB stars in the field, the black dots show RGB stars within the masked region not included in our analysis. In this figure, north is up and east is to the left.

from BST1047 is also not a concern; as shown in J. C. Mihos et al. (2024), BST1047 has no old stellar population, and the distribution of RGB stars across the full (unmasked) ACS field appears quite uniform (as also shown in Figure 9 of

J. C. Mihos et al. 2024), rather than being clustered near BST1047.

Another complication to our study of M96 halo populations is the group environment—specifically, the possibility of contamination by intragroup stars stripped from other galaxies in the group. The presence of stellar streams in the intragroup light could lead to field-to-field variations in the inferred density of the stellar halo and in the ages or metallicities of the stellar populations. However, deep imaging of the Leo I group shows little evidence for intragroup light around M96 down to a limit of $\mu_V = 29.5$ mag arcsec^{-2} (A. E. Watkins et al. 2014). We also see no differences in the spatial density or F606W − F814W colors of the RGB stars in our two fields that probe the M96 halo. We do, however, see a modest north–south gradient in the density of RGB stars across the WFC3 field (shown in Figure 3). This gradient, while modest, appears statistically significant. We can compare the spatial distribution of the data to that for a uniform distribution using the σ/total metric of E. F. Bell et al. (2008), which calculates the variation in counts across spatial bins compared to the uniform distribution, while properly factoring in the Poisson sampling statistics of the data. Breaking the WFC3 field into quadrants to measure the statistic, we find $\sigma/\text{total} = 0.52 \pm 0.03$ (compared to values of $\sigma/\text{total} = 0.2 \pm 0.1$ for a purely random distribution), arguing that the gradient is real and may be tracing substructure around M96; however, this gradient is weak, and additional deep fields around M96 would be necessary to test the field-to-field variation in RGB surface density more robustly.

Comparing the RGB stars in the ACS and WFC3 fields, both show a broad color spread, indicative of a range of metallicities in the stellar populations. The stars in the RGB selection box for the ACS field show a median color of F606W − F814W=1.05 ± 0.02 (where the error bar comes from bootstrap resampling of the data), while those in the WFC3 field show a median color of F606W − F814W=1.07 ± 0.02. The difference in median color is very small and consistent with the uncertainty in the relative photometric zero-point differences between the WFC3 and ACS cameras (S. E. Deustua & J. Mack 2018). Both fields also show very similar color spreads. The RGB stars in the ACS field show an F606W − F814W interquartile spread of 0.20 mag, compared to a spread of 0.19 mag in the WFC3 field. This color spread is significantly larger than the photometric color uncertainty at these magnitudes (≈0.07 and 0.10 for ACS and WFC3, respectively) and thus reflects a true underlying metallicity spread in the stellar populations. The similarities in the median color and color spread between the two fields argue that both fields are tracing similar stellar populations.

With no discernible difference in the color distributions of the two fields, we combine the ACS and WFC3 photometry and replot them together in Figure 4(a), overlaying Parsec 1.2S isochrones (A. Bressan et al. 2012; P. Marigo et al. 2017) for 10 Gyr old stellar populations spanning a range of metallicity [M/H] = −2.0 to 0.0. Although we are largely insensitive to stars of solar metallicity, we see little evidence for stars of metallicity higher than [M/H] = −0.5. There are very few stars in the CMD redward of F606W − F814W = 1.5, and what few stars are there are consistent with the expectations for contaminants from the A2744FF data (Figure 2).

We use these isochrones to estimate the metallicity distribution function (MDF) for the M96 halo populations. We first select all point sources in the RGB selection box shown in Figure 4(a), which has been expanded redward compared to that shown in Figure 2, to account for any metal-rich population. Then, using a grid of finely interpolated Parsec isochrones of age 10 Gyr and spanning the range [M/H] = −2.2 to −0.2, for each observed RGB star we locate the closest model isochrone and assign the star the metallicity of that isochrone. We account for photometric uncertainty by repeating this process 100 times, each time randomly scattering the isochrone points in color and magnitude by adding a Gaussian random error based on the photometric uncertainty model. To correct for contamination, we run an identical analysis on sources in the A2744FF field and subtract the resulting MDF from that derived from the combined ACS and WFC3 photometry. We show the derived background-corrected MDF for M96's halo in Figure 4(b), along with the background correction inferred from the A2744FF data.

The M96 halo MDF shows a broad distribution in metallicity spanning the range $-2.2 \leqslant [M/H] \leqslant -0.3$. The sharp cutoff at [M/H] = −2.2 is formally due to the lack of isochrones at lower metallicities, but we also note that at these extremely low inferred metallicities, the true counts have greater uncertainty, due to increasing contamination from unresolved background galaxies on the blue side of the RGB selection box. The amount of contamination in this region of the CMD is highly sensitive to the exact details of how sources are selected using the DOLPHOT SHARP cuts described in Section 2 and is reflected in the increased contamination correction at very low metallicity inferred from the A2744FF field as well (the red histogram in Figure 4(b)). Thus, we do not place much significance on this lowest-metallicity bin in the derived MDF. If we exclude this bin from the analysis of the MDF, we find a median metallicity for the M96 halo of [M/H] = −1.36, with an interquartile spread of 0.75 dex. This metallicity is similar to that found in the outer halos of other spiral galaxies (B. Harmsen et al. 2017; C. Conroy et al. 2019; A. Smercina et al. 2020), and we discuss this more fully in Section 4 below.

We estimate the uncertainty in the inferred median metallicity in two ways. First, to estimate the random errors, we run a bootstrap analysis, calculating the median metallicity on 100 subsamples of the RGB stars randomly drawn (with replacement) from the full RGB sample; we find a random error in the median of ≈±0.05 dex. Systematic uncertainties are harder to assess. As one example, we recalculate the metallicities using isochrones that vary in age from 6 Gyr to 12 Gyr and find that the derived median metallicity varies along this sequence from [M/H] = −1.19 to −1.40. Alternatively, we can bypass the model isochrones and instead use the color–metallicity calibration of D. Streich et al. (2014; based on the metallicities of Galactic globular clusters) to convert the median F606W − F814W color of the RGB stars to metallicity. Using the D. Streich et al. (2014) calibration at an absolute F814W magnitude of $M_{\rm F814W} = -3.5$ (F814W = 26.7), we get [M/H] = −1.42, while using the $M_{\rm F814W} = -3.0$ calibration, we get [M/H] = −1.20. These calculations suggest a *minimum* systematic uncertainty of ±0.1 dex and likely even higher (see, e.g., the discussion in D. Streich et al. 2014).

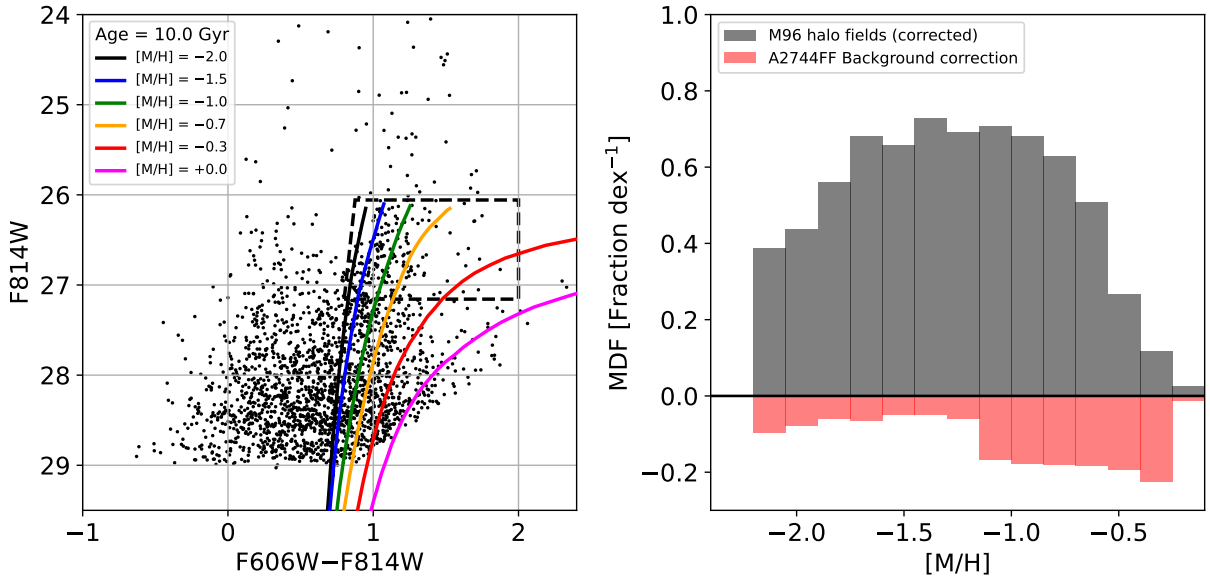

Figure 4. Left: the CMD for the combined ACS and WFC3 fields, overlaid with 10 Gyr old Parsec 1.2S isochrones (A. Bressan et al. 2012; P. Marigo et al. 2017) of varying metallicity. Right: the inferred M96 halo MDF for the RGB population selected from stars in the dashed box of the CMD. The halo MDF has been corrected for background contamination, based on an analysis of similarly selected sources in the A2744FF photometry, shown in red. See the text for details.

4. Discussion

Our imaging of the outer halo of M96 has revealed a sparse population of old RGB stars with a broad range of metallicity at a galactocentric distance of 50 kpc. While the ACS and WFC3 fields do not sample different halo radii, they are separated by about 19 kpc and can probe the uniformity of the halo stellar populations. We find little variation in their properties, however. Both fields have similar stellar densities (11.7 arcsec^{-2} versus 11.4 arcsec^{-2} for ACS and WFC3, respectively, after background correction), median RGB color (1.05 versus 1.07), and RGB color quartile spread (0.20 versus 0.19), with all values agreeing to well within the uncertainties. There is some evidence for a weak north–south gradient in RGB counts in the WFC3 field (see Figure 3), but aside from that possibility, we find no obvious evidence for substructure in the stellar populations.

We can use the counts to estimate the equivalent projected surface brightness of the halo. Using the PARSEC isochrones for an old (10 Gyr) metal-poor ([M/H] $= -1.3$) stellar population, and scaling in mass to match the RGB number counts seen in our imaging fields, we derive an equivalent surface brightness of $\mu_V \approx 31.7$ mag arcsec^{-2} for these fields. This is consistent with the nondetection of diffuse light in this region by A. E. Watkins et al. (2014), since the equivalent surface brightness derived from our HST imaging is significantly fainter than the A. E. Watkins et al. (2014) surface brightness limit of $\mu_V \approx 29.5$ mag arcsec^{-2}.

To test how well the M96 stellar halo follows the stellar halo mass–metallicity relationship for spiral galaxies, we need an estimate of M96's stellar halo mass. Previous studies (e.g., B. Harmsen et al. 2017; K. Gozman et al. 2023) have typically measured this by using data taken at different radii to derive the halo density profile, then integrating that projected profile from 10–40 kpc (to avoid contamination from the bright inner regions of the galaxy). However, without fields spanning a range of radii, we cannot characterize the halo density profile, so instead we adopt a power-law profile for the projected stellar density, given by $\Sigma(R) = \Sigma(R_0)(R/R_0)^{\alpha}$. Parameterized in this way, spiral galaxies show an observed variety of halo profile slopes spanning the range $\alpha = -2$ to -4 (A. J. Deason et al. 2011; K. M. Gilbert et al. 2012; R. A. Ibata et al. 2014; B. Harmsen et al. 2017; J. T. Mackereth & J. Bovy 2020; A. Smercina et al. 2020; K. Gozman et al. 2023). The integrated mass will also depend on the flattening of the halo—but again, with only two fields projected along the minor axis of M96, we cannot measure the halo flattening. Instead, we adopt a projected axis ratio of $b/a = 0.6$, similar to the observed axis ratios for stellar halos around nearby spirals (B. Harmsen et al. 2017). Normalizing the profile to our measured projected density at 50 kpc ($\Sigma = 11.65$ RGB stars arcmin^{-2}), we then integrate the profile over the radial range corresponding to 10–40 kpc in projection to derive a halo mass over that radial range of $M_{h,10-40} = 2.6^{+5.8}_{-1.7} \times 10^9 M_{\odot}$, where the error bar shows the effect of varying the profile slope over the range $\alpha = -2$ to -4. We also note that simulations suggest some correlation between the halo density profile slope and accretion history (A. Monachesi et al. 2019), so the range of slope we consider can also be considered as spanning a range of accretion scenarios. Finally, we need to convert the $M_{h,10-40}$ halo mass to a total stellar halo mass. We follow the conversion from B. Harmsen et al. (2017), who used the properties of simulated stellar halos in J. S. Bullock & K. V. Johnston (2005) to show the total stellar halo mass is roughly a factor of 3 larger than $M_{h,10-40}$. Using this scaling factor, we ultimately derive a total stellar halo mass for M96 of $M_{h,tot} = 7.8^{+17.4}_{-4.9} \times 10^9 M_{\odot}$.

We use this estimate of the halo mass to put M96 onto the halo mass–halo metallicity relationship shown in Figure 5, using the data from K. Gozman et al. (2023), which add galaxies to the previous relationships derived by B. Harmsen et al. (2017) and A. Smercina et al. (2022). In our M96 data point, the metallicity error bar reflects a combination of the ± 0.05 dex random uncertainty and the ± 0.10 minimum systematic uncertainty discussed in Section 3. Our M96 measurement falls well below the mean relationship, by ≈ 0.7 dex in metallicity. Given the tight scatter in the

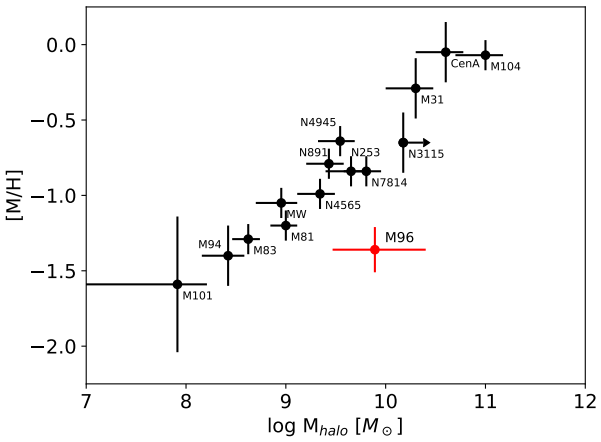

Figure 5. The halo mass–halo metallicity relationship from K. Gozman et al. (2023), with our measurement of M96 added. Note that the metallicity measurements for the K. Gozman et al. (2023) points are measured at 30 kpc, while our fields in M96 are at a larger projected distance of 50 kpc.

K. Gozman et al. (2023) dataset, the offset of M96 from the other galaxies is quite significant.

A variety of factors may contribute to this displacement of M96 from the mean relationship between halo mass and metallicity. First, our metallicity measurement is made at a projected radius of 50 kpc, while the other galaxies in the plot are measured at 30 kpc. If there is an appreciable metallicity gradient in M96's halo, this would push the M96 point upward, more in line with the other galaxies. While spiral galaxy halos show a range of metallicity gradients, to completely explain the offset a substantial gradient would be needed (≈ -0.035 dex kpc^{-1}), much larger than is typically seen (e.g., K. M. Gilbert et al. 2014; A. Monachesi et al. 2016; K. Gozman et al. 2023). Another concern is that our estimated halo mass may be too high. With only two closely separated fields, our mass estimate is based on assumptions about both the halo density slope and its projected flattening. A shallower slope and/or rounder halo would reduce the inferred mass and again bring M96 more into alignment. Finally, we do see some evidence for substructure in the projected counts, particularly in the WFC3 field. If our fields happen to sample discrete tidal streams, either in M96's halo or perhaps in the Leo I group intragroup environment, this could again lead to an overestimate of M96's halo mass and potentially also bias the inferred metallicity in either direction. Indeed, some combination of all three of these effects—metallicity gradient, halo density profile, and tidal substructure—could work together to move M96 back toward the mean relationship; imaging of the stellar populations in additional fields around M96 would be necessary to assess these variations.

However, if our estimates of the mass and metallicity of M96's halo should be confirmed, this would suggest that more scatter in the spiral halo mass–metallicity relation exists than previously realized. As the mass–metallicity relationship is often interpreted in the context of the accretion-driven growth of stellar halos (see, e.g., R. D'Souza & E. F. Bell 2018a; A. Monachesi et al. 2019; A. Smercina et al. 2022), this would in turn imply differences in the assembly history of M96 compared to other spirals. For example, M96 may have suffered a major merger particularly early in its history, accreting a massive but relatively metal-poor satellite to build its halo mass without a concurrent increase in metallicity. Alternatively, over its history, M96 may have accreted a particularly large number of low-mass, metal-poor satellites, growing a massive but metal-poor stellar halo more gradually over time. The fact that stellar halos reflecting such scenarios are not commonly seen in simulations (R. D'Souza & E. F. Bell 2018a; A. Monachesi et al. 2019) would suggest that these are uncommon evolutionary paths, consistent with M96's offset from the otherwise relatively tight correlation between halo mass and metallicity. Finally, while it may be tempting to consider M96's presence in the active Leo I group environment as shaping an alternative evolutionary path, we note that many of the galaxies that define the mass–metallicity relationship seen in Figure 5 are also found in group environments, including M101, M81, and of course the Milky Way and Andromeda.

While the metallicity distribution shown in Figure 4 is broad, it is not unreasonably so for the halo of a large spiral galaxy built up through accretion. For example, in the Auriga galaxy formation simulations (R. J. J. Grand et al. 2017), the outer regions of spiral galaxy halos show a wide range of metallicities, with individual halos showing a 10%–90% metallicity spread of 1 dex or more (A. Monachesi et al. 2019; A. Fattahi et al. 2020), compared to the 10%–90% metallicity spread of 1.1 dex that we find in M96. The observed MDFs for stars in spiral galaxy halos also tend to be broad (e.g., M. Mouhcine et al. 2005b, 2007; M. Rejkuba et al. 2009; D. Carollo et al. 2010; R. A. Ibata et al. 2014).

Alternatively, we can directly compare the F606W − F814W color spread of our M96 halo stars to the colors observed in other spiral galaxy halos by the GHOSTS team (A. Monachesi et al. 2016). By comparing RGB star colors, we alleviate systematic effects due to the transformation of colors to metallicity. To calculate the color spread in the GHOSTS sample, A. Monachesi et al. (2016) define a color quantity known as the "Q-index color," which essentially rotates the CMD so that the metal-poor RGB sequence is vertical in the rotated CMD. Done this way, the Q-index then minimizes the effect of the tilt of the RGB in the CMD on the derived color spread. Selecting RGB samples that vary in depth from 0.5 to 2 mag below the TRGB, A. Monachesi et al. (2016) find Q-index spreads (16%–84%) of 0.25–0.5 mag for the halos in the GHOSTS sample. For our M96 measurement, we select stars up to 1 magnitude below the tip ($m_{\rm tip,F814W} = 26.2$) and in the color range $1.0 \leqslant$ F606W − F814W $\leqslant 1.4$, similar to the range used by A. Monachesi et al. (2016), and derive a Q-index spread of 0.27 mag for the M96 halo. This similarity in color spread between M96 and the GHOSTS halos again argues that the spread of metallicities in M96's halo is typical of spiral galaxies in general.

Finally, we can also use our estimate of M96's stellar halo mass ($M_{\rm tot,halo} = 7.8^{+17.4}_{-4.9} \times 10^9 M_\odot$) to estimate the stellar halo mass fraction ($M_{*,\rm halo}/M_{*,\rm gal}$). If we adopt a total stellar mass for M96 of $M_{*,\rm gal} = 5.3 \times 10^{10} M_\odot$, from the Spitzer Survey of Stellar Structure in Galaxies (S4G, K. Sheth et al. 2010; J. C. Muñoz-Mateos et al. 2013; M. Querejeta et al. 2015), we derive a stellar halo mass fraction of 15^{+33}_{-9}%. Spiral galaxies show a wide variation in halo mass fraction, ranging from $\leqslant$1% for galaxies such as M101 (A. Merritt et al. 2016; I. S. Jang et al. 2020) to a few percent for the Milky Way and M81 (e.g., A. J. Deason et al. 2019; I. S. Jang et al. 2020; J. T. Mackereth & J. Bovy 2020; A. Smercina et al. 2020) to 10% or more for galaxies such as M31, NGC 1084, and

NGC 3368 (E. F. Bell et al. 2017; B. Harmsen et al. 2017; A. Smercina et al. 2022). Simulations of stellar halos formed through accretion also show a wide range of mass fractions (A. P. Cooper et al. 2013; A. Monachesi et al. 2019). Conversely, while M96 appears to fall in the upper range of halo mass *fractions* for a large spiral galaxy, its stellar halo itself is not anomalously massive. The total stellar halo mass of the Milky Way (and M81) is smaller, $\sim 10^9 M_\odot$ (J. T. Mackereth & J. Bovy 2020; A. Smercina et al. 2020), while M31 has a larger total stellar halo mass of $M_{*,\rm halo} \sim 10^{10} M_\odot$ (R. A. Ibata et al. 2014; B. Harmsen et al. 2017). Although our uncertainties are rather large, it thus appears that M96 has a stellar halo mass that is intermediate between these "more typical" spiral galaxies.

5. Summary

We have used deep HST ACS and WFC3 imaging in F606W/F814W to study the resolved stellar populations in the outer halo of the spiral galaxy M96, at a projected radius of 50 kpc from the galaxy's center. Our imaging probes nearly 2 magnitudes below the expected TRGB, and in both fields we clearly detect RGB stars at a surface density (over the expected background) of ≈ 11.65 arcmin^{-2}. Comparing the properties of the RGB stars in each field, we find no significant differences in their surface density or their mean F606W − F814W color or quartile color spread.

Combining the photometry from the two fields, we then use stellar isochrones to derive the MDF for the RGB stars. We find a median metallicity of [M/H] = −1.36, with a quartile spread of 0.75 dex. At this metallicity, the equivalent surface brightness of M96's halo is $\mu_V \approx 31.7$ mag arcsec^{-2}—well below the upper limits on the M96 halo surface brightness from deep imaging of the Leo I group by A. E. Watkins et al. (2014). Assuming a power-law profile for the projected radial density of the halo, we derive a total halo mass of $\approx 7.8^{+17.4}_{-4.9} \times 10^9 M_\odot$, approximately 15^{+33}_{-9}% of the total stellar mass of the galaxy.

With our estimates of the halo mass and metallicity in hand, we place M96 on the stellar halo mass–metallicity relationship and find the galaxy falls significantly below that relationship. Compared to other nearby spiral galaxies, M96 appears to have a relatively metal-poor halo (by ∼0.7 dex) for its halo mass. While the low metallicity we find for M96's halo may be partly explained by the larger radius we probe (compared to other galaxies that define that relationship), additional systematic effects may be at work, including uncertainties in our adopted halo mass profile and the possibility that we are sampling underlying tidal streams in M96's halo or the Leo I intragroup environment. These systematic uncertainties aside, if our result should be confirmed, it would imply that the accretion path that built M96's halo may be systematically different from that inferred for other spirals in the nearby Universe. Possibilities for building up a massive metal-poor halo for M96 include a very early merger with a massive but low-metallicity companion or a more gradual accretion of a large number of low-mass, metal-poor satellites.

Furthermore, while it may be tempting to ascribe M96's outlier status to its ongoing interactions within the dynamically active Leo I group, it is not obvious that this is correct. To illustrate this, an interesting comparison can be made between M96, M81, and M101. All three of these galaxies live in active group environments and have had recent interactions within the past few hundred Myr—M96, as traced by the stellar populations in BST1047 (J. C. Mihos et al. 2024); M81 with M82 and NGC3077 (M. S. Yun et al. 1994); and M101 with NGC 5474 (S. T. Linden & J. C. Mihos 2022). While all three are experiencing recent interactions, M101 and M81 both adhere to the halo stellar-mass–metallicity relationship seen in Figure 5, while M96 remains an outlier. This result reinforces the idea that the halo properties of galaxies are likely more sensitive to their integrated accretion history than to their immediate dynamical environment.

The main limitation of our study of the M96 stellar halo is the sparseness of our imaging data. With only two fields surveyed, both at similar galactocentric distance from M96, we cannot derive a radial density profile nor can we test for the presence of substructure in the halo. While both our fields have similar stellar populations and surface densities, we see some spatial variation in the form of a weak density gradient in the WFC3 field. Whether or not this is signaling a larger degree of underlying substructure is unclear, and further imaging of the stellar populations in the field around M96—and throughout the Leo I group as a whole—would shed new light on the role interactions and accretion play in shaping the halos of spiral galaxies.

Acknowledgments

The authors would like to thank Christian Soto and Norman Grogin for their help with planning and refining the HST observations. We also thank Adam Smercina and Katya Gozman for useful discussions and for providing in digital form the data used in Figure 5. We also thank the anonymous referee for suggestions that significantly improved our presentation of the results. This research is based on observations made with the NASA/ESA Hubble Space Telescope for program #GO-16762 and obtained at the Space Telescope Science Institute (STScI). STScI is operated by the Association of Universities for Research in Astronomy, Inc., under NASA contract NAS5-26555. Support for this program was provided by NASA through grants to J.C.M. and P.R.D. from STScI. A.E.W. acknowledges support from the STFC (grant Nos. ST/Y001257/1 and ST/X001318/1).

Facilities: HST (ACSWFC3). The HST imaging data used in this study can be accessed at the Mikulski Archive for Space Telescopes (MAST) at STScI via WFC3). The HST imaging data used in this study can be accessed at the Mikulski Archive for Space Telescopes (MAST) at STScI via doi:10.17909/300a-ns91.

Software: astropy (The Astropy Collaboration et al. 2013, 2022; The Astropy Collaboration 2018), DOLPHOT (A. E. Dolphin 2000), numpy (C. R. Harris et al. 2020), matplotlib (J. D. Hunter 2007), photutils (L. Bradley et al. 2025), scipy (P. Virtanen et al. 2020).

ORCID iDs

J. Christopher Mihos https://orcid.org/0000-0002-7089-8616
Patrick R. Durrell https://orcid.org/0000-0001-9427-3373
Aaron E. Watkins https://orcid.org/0000-0003-4859-3290

References

Bailin, J., Bell, E. F., Chappell, S. N., et al. 2011, ApJ, 736, 24
Barker, M. K., Ferguson, A. M. N., Irwin, M., et al. 2009, AJ, 138, 1469

Bell, E. F., Monachesi, A., Harmsen, B., et al. 2017, ApJL, 837, L8
Bell, E. F., Zucker, D. B., Belokurov, V., et al. 2008, ApJ, 680, 295
Belokurov, V., Erkal, D., Evans, N. W., et al. 2018, MNRAS, 478, 611
Belokurov, V., Zucker, D. B., Evans, N. W., et al. 2006, ApJL, 642, L137
Bonaca, A., & Price-Whelan, A. M. 2025, NewAR, 100, 101713
Bradley, L., Sipőcz, B., Robitaille, T., et al. 2025, astropy/photutils, v.2.3.0, Zenodo, doi:10.5281/zenodo.17129028
Bressan, A., Marigo, P., Girardi, L., et al. 2012, MNRAS, 427, 127
Bullock, J. S., & Johnston, K. V. 2005, ApJ, 635, 931
Carollo, D., Beers, T. C., Chiba, M., et al. 2010, ApJ, 712, 692
Carollo, D., Beers, T. C., Lee, Y. S., et al. 2007, Natur, 450, 1020
Chonis, T. S., Martínez-Delgado, D., Gabany, R. J., et al. 2011, AJ, 142, 166
Cohen, R. E., Goudfrooij, P., Correnti, M., et al. 2020, ApJ, 890, 52
Conroy, C., Naidu, R. P., Zaritsky, D., et al. 2019, ApJ, 887, 237
Cooper, A. P., Cole, S., Frenk, C. S., et al. 2010, MNRAS, 406, 744
Cooper, A. P., D'Souza, R., Kauffmann, G., et al. 2013, MNRAS, 434, 3348
Crnojević, D. 2017, ASSL, 434, 31
De Lucia, G., & Helmi, A. 2008, MNRAS, 391, 14
Deason, A. J., & Belokurov, V. 2024, NewAR, 99, 101706
Deason, A. J., Belokurov, V., & Evans, N. W. 2011, MNRAS, 416, 2903
Deason, A. J., Belokurov, V., Evans, N. W., et al. 2013, ApJ, 763, 113
Deason, A. J., Belokurov, V., & Sanders, J. L. 2019, MNRAS, 490, 3426
Deason, A. J., Mao, Y.-Y., & Wechsler, R. H. 2016, ApJ, 821, 5
Deustua, S. E., & Mack, J. 2018, Comparing the ACS/WFC and WFC3/UVIS Calibration and Photometry Instrument Science Report WFC3 2018-02, Space Telescope Science Institute https://www.stsci.edu/files/live/sites/www/files/home/hst/instrumentation/wfc3/documentation/instrument-science-reports-isrs/_documents/2018/WFC3-2018-02.pdf
Dey, A., Najita, J. R., Koposov, S. E., et al. 2023, ApJ, 944, 1
Dolphin, A. E. 2000, PASP, 112, 1383
D'Souza, R., & Bell, E. F. 2018a, MNRAS, 474, 5300
D'Souza, R., & Bell, E. F. 2018b, NatAs, 2, 737
Durrell, P. R., Sarajedini, A., & Chandar, R. 2010, ApJ, 718, 1118
Elias, L. M., Sales, L. V., Creasey, P., et al. 2018, MNRAS, 479, 4004
Fattahi, A., Deason, A. J., Frenk, C. S., et al. 2020, MNRAS, 497, 4459
Font, A. S., Johnston, K. V., Bullock, J. S., et al. 2006, ApJ, 638, 585
Gilbert, K. M., Guhathakurta, P., Beaton, R. L., et al. 2012, ApJ, 760, 76
Gilbert, K. M., Kalirai, J. S., Guhathakurta, P., et al. 2014, ApJ, 796, 76
Gilbert, K. M., Quirk, A. C. N., Guhathakurta, P., et al. 2022, ApJ, 924, 116
Gilhuly, C., Merritt, A., Abraham, R., et al. 2022, ApJ, 932, 44
Gozman, K., Bell, E. F., Smercina, A., et al. 2023, ApJ, 947, 21
Graham, J. A., Phelps, R. L., Freedman, W. L., et al. 1997, ApJ, 477, 535
Grand, R. J. J., Gómez, F. A., Marinacci, F., et al. 2017, MNRAS, 467, 179
Greggio, L., Rejkuba, M., Gonzalez, O. A., et al. 2014, A&A, 562, A73
Harmsen, B., Bell, E. F., D'Souza, R., et al. 2023, MNRAS, 525, 4497
Harmsen, B., Monachesi, A., Bell, E. F., et al. 2017, MNRAS, 466, 1491
Harris, C. R., Millman, K.J., van der Walt, S.J., et al. 2020, Natur, 585, 357
Helmi, A. 2020, ARA&A, 58, 205
Helmi, A., Babusiaux, C., Koppelman, H. H., et al. 2018, Natur, 563, 85
Hunter, J. D. 2007, CSE, 9, 90
Ibata, R., Chapman, S., Ferguson, A. M. N., et al. 2004, MNRAS, 351, 117
Ibata, R., Irwin, M., Lewis, G., et al. 2001, Natur, 412, 49
Ibata, R., Martin, N. F., Irwin, M., et al. 2007, ApJ, 671, 1591
Ibata, R. A., Lewis, G. F., McConnachie, A. W., et al. 2014, ApJ, 780, 128
Jang, I. S., de Jong, R. S., Holwerda, B. W., et al. 2020, A&A, 637, A8
Kalirai, J. S., Gilbert, K. M., Guhathakurta, P., et al. 2006, ApJ, 648, 389
Kang, J., Kim, Y. J., Lee, M. G., et al. 2020, ApJ, 897, 106
Lee, M. G., & Jang, I. S. 2016, ApJ, 822, 70
Linden, S. T., & Mihos, J. C. 2022, ApJL, 933, L33
Lotz, J. M., Koekemoer, A., Coe, D., et al. 2017, ApJ, 837, 97
Mackereth, J. T., & Bovy, J. 2020, MNRAS, 492, 3631
Malin, D., & Hadley, B. 1997, PASA, 14, 52
Marigo, P., Girardi, L., Bressan, A., et al. 2017, ApJ, 835, 77
Martin, N. F., Ibata, R. A., Rich, R. M., et al. 2014, ApJ, 787, 19
Martin, N. F., Ibata, R. A., Starkenburg, E., et al. 2022, MNRAS, 516, 5331
Martínez-Delgado, D., Cooper, A. P., Román, J., et al. 2023, A&A, 671, A141
Martínez-Delgado, D., Gabany, R. J., Crawford, K., et al. 2010, AJ, 140, 962
McConnachie, A. W., Ibata, R., Martin, N., et al. 2018, ApJ, 868, 55
McConnachie, A. W., Irwin, M. J., Ibata, R. A., et al. 2009, Natur, 461, 66
Merritt, A., van Dokkum, P., Abraham, R., et al. 2016, ApJ, 830, 62
Michel-Dansac, L., Duc, P.-A., Bournaud, F., et al. 2010, ApJL, 717, L143
Mihos, J. C., Carr, C. T., Watkins, A. E., et al. 2018, ApJL, 863, L7
Mihos, J. C., Durrell, P. R., Feldmeier, J. J., et al. 2018, ApJ, 862, 99
Mihos, J. C., Durrell, P. R., Toloba, E., et al. 2022, ApJ, 924, 87
Mihos, J. C., Durrell, P. R., Watkins, A. E., et al. 2024, ApJ, 964, 67
Monachesi, A., Bell, E. F., Radburn-Smith, D. J., et al. 2016, MNRAS, 457, 1419
Monachesi, A., Gómez, F. A., Grand, R. J. J., et al. 2019, MNRAS, 485, 2589
Mouhcine, M., Ferguson, H. C., Rich, R. M., et al. 2005a, ApJ, 633, 821
Mouhcine, M., Rejkuba, M., & Ibata, R. 2007, MNRAS, 381, 873
Mouhcine, M., Rich, R. M., Ferguson, H. C., et al. 2005b, ApJ, 633, 828
Muñoz-Mateos, J. C., Sheth, K., Gil de Paz, A., et al. 2013, ApJ, 771, 59
Naidu, R. P., Conroy, C., Bonaca, A., et al. 2020, ApJ, 901, 48
Ogami, I., Tanaka, M., Komiyama, Y., et al. 2025, MNRAS, 536, 530
Oosterloo, T., Morganti, R., Crocker, A., et al. 2010, MNRAS, 409, 500
Pillepich, A., Vogelsberger, M., Deason, A., et al. 2014, MNRAS, 444, 237
Querejeta, M., Meidt, S. E., Schinnerer, E., et al. 2015, ApJS, 219, 5
Radburn-Smith, D. J., de Jong, R. S., Seth, A. C., et al. 2011, ApJS, 195, 18
Rejkuba, M., Harris, W. E., Greggio, L., et al. 2022, A&A, 657, A41
Rejkuba, M., Mouhcine, M., & Ibata, R. 2009, MNRAS, 396, 1231
Robin, A. C., Reylé, C., Derrière, S., et al. 2003, A&A, 409, 523
Schlafly, E. F., & Finkbeiner, D. P. 2011, ApJ, 737, 103
Schneider, S. 1985, ApJL, 288, L33
Schneider, S. E., Salpeter, E. E., & Terzian, Y. 1986, AJ, 91, 13
Shang, Z., Zheng, Z., Brinks, E., et al. 1998, ApJL, 504, L23
Sheth, K., Regan, M., Hinz, J. L., et al. 2010, PASP, 122, 1397
Smercina, A., Bell, E. F., Price, P. A., et al. 2020, ApJ, 905, 60
Smercina, A., Bell, E. F., Samuel, J., et al. 2022, ApJ, 930, 69
Sotillo-Ramos, D., Pillepich, A., Donnari, M., et al. 2022, MNRAS, 516, 5404
Streich, D., de Jong, R. S., Bailin, J., et al. 2014, A&A, 563, A5
Tanaka, M., Chiba, M., Komiyama, Y., et al. 2010, ApJ, 708, 1168
Taylor, R., Köppen, J., Jáchym, P., et al. 2022, AJ, 164, 233
The Astropy Collaboration 2018, AJ, 156, 123
The Astropy Collaboration, Price-Whelan, A. M., Lim, P. L., et al. 2022, ApJ, 935, 167
The Astropy Collaboration, Robitaille, T. P., Tollerud, E. J., et al. 2013, A&A, 558, A33
Virtanen, P., Gommers, R., Oliphant, T. E., et al. 2020, NatMe, 17, 261
Watkins, A. E., Mihos, J. C., Harding, P., et al. 2014, ApJ, 791, 38
Wempe, E., Helmi, A., White, S. D. M., et al. 2025, A&A, 701, A178
Yun, M. S., Ho, P. T. P., & Lo, K. Y. 1994, Natur, 372, 530